ACS APPLIED MATERIALS & INTERFACES

Research Article

www.acsami.org

Self-Organized Macroporous Carbon Structure Derived from Phenolic Resin via Spray Pyrolysis for High-Performance Electrocatalyst

Ratna Balgis,[†] Sumihito Sago,[†,‡] Gopinathan M. Anilkumar,[‡] Takashi Ogi,*[,†] and Kikuo Okuyama[†]

[†]Department of Chemical Engineering, Graduate School of Engineering, Hiroshima University, 1-4-1 Kagamiyama, Higashi-Hiroshima 739-8527, Japan

[‡]Research and Development Center, Noritake Co., Ltd., 300 Higashiyama, Miyoshi, Aichi 470-0293, Japan

ABSTRACT: The synthesis and evaluation of porous carbon derived from phenolic resin using a fast and facile spray pyrolysis method has been studied for use as a new electrocatalyst support material. By adding polystyrene latex nanoparticles as a template to the phenolic resin precursor, self-organized macroporous carbon structure was first developed. The mass ratio of phenolic resin to PSL at 0.625 gave the optimum porous morphology. Pt nanoparticles (~20 wt %) were grown on the carbon surface using a standard industrial impregnation method. Well-dispersed Pt nanoparticles of average size 3.91 nm were observed on the surface of porous carbon particles. The high catalytic performance of porous Pt/C electrocatalyst was confirmed by the high mass activity and electrochemically active surface area, which were 450.81 mA mg^{-1}-Pt and 81.78 m^2 g^{-1}-Pt, respectively. The porous Pt/C catalyst obtains two times higher mass activity than that of the commercial Pt/C catalyst and performs excellent durability under acid conditions.

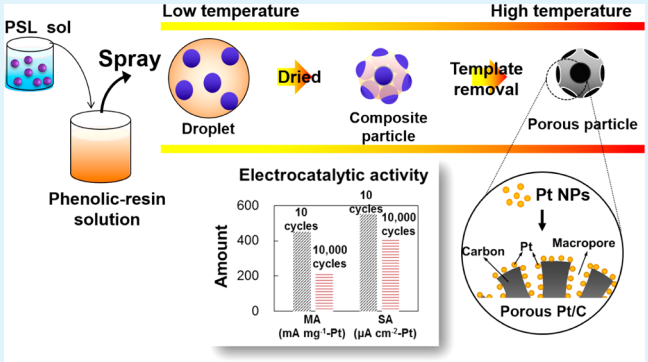

KEYWORDS: *phenolic-resin, macroporous, spray pyrolysis, electrocatalyst, mass activity, durability*

1. INTRODUCTION

The performance of an electrocatalyst relies strongly on its support material.[1−3] The design of electrocatalyst support materials therefore plays a crucial role in determining the overall electrocatalytic performance. The successful design of electrocatalyst support materials gives high-performance and reliable electrocatalysts.[4−7] Several types of electrocatalyst support materials are currently being studied such as carbonaceous materials, metal oxides, and nitrides.[8−13]

Carbonaceous materials are favored because of the natural abundance of carbon, and they can be easily synthesized by the carbonization of various organic materials.[14,15] Much recent interest has been shown in the development of carbon-based catalysts produced using carbon black materials, such as Vulcan carbon, as a catalyst support.[16−18] The entire surface of Vulcan carbon is decorated with micropores giving a very high specific surface area ~250 m^2/g and large pore volume.[19,20] Although such microporous materials are used in catalysis applications, they have limitations arising from the slow mass transport of molecules because of space confinement imposed by small pore sizes, low conductivity arising from the presence of large numbers of surface functional groups and defects, and the collapse of porous structures in the harsh environment of proton exchange membrane fuel cell (PEMFC) operation, which potentially trap and inactivate Pt nanoparticles.[21]

Carbonaceous materials derived from organic materials offer morphological control by simply adding a specific template.[22−26] However, the carbonization ratios of such materials are quite low, resulting in high-cost mass production. Recently, it has been found that inexpensive phenolic resin is more attractive as a carbon source because it has a high carbonization ratio.[27,28]

The structural engineering of carbonaceous materials to give ultrafine spherical particles can be rapidly obtained using spray pyrolysis methods.[29] The use of silica as a sacrificial template for preparing hollow spherical carbon particles from phenolic resin by spray pyrolysis has been reported.[30] However, the functionalization of phenolic resin derived carbon particles has not yet been addressed. Functionalization of the controlled morphology of phenolic resin derived carbon for use as catalyst supports will provide more active Pt Nanoparticles and improve the chemical properties of the catalyst that will give catalysts exhibiting high electrocatalytic performances and good durabilities.

To the best of our knowledge, there have been no previous reports of the preparation of high-performance electrocatalysts

Received: August 30, 2013
Accepted: October 30, 2013
Published: October 30, 2013

consisting of Pt-nanoparticle-decorated macroporous carbon particles (porous Pt/C), derived from a phenolic resin via spray pyrolysis. Sacrificial template particles, i.e., polystyrene latexes (PSL) that decompose easily during carbonization, were chosen to control the morphology of the produced particles.[4] The obtained layered pores, which create channels inside the particles, could support a three-phase boundary (i.e. ion conducting phase, electron conducting phase, and gas phase). The use of multistep stacking of temperature zones in the spray pyrolysis reactor controls the formation of the phenolic resin/PSL composite and the carbonization process. Morphological control of the carbon was investigated in detail by changing the ratio of phenolic resin to PSL. We carried out cyclic voltammetry (CV) and an oxygen reduction reaction (ORR) on the materials to determine their electrochemical properties.

2. EXPERIMENTAL SECTION

2.1. Preparation of Porous Pt/C Electrocatalyst. An aqueous solution containing phenolic resin (Sumitomo Bakelite Co., Ltd., Tokyo, Japan) and 4 wt % of laboratory-produced PSL (230 nm) beads were used as a precursor to prepare carbon particles by spray pyrolysis. The spray pyrolysis apparatus consisted of an ultrasonic nebulizer (1.7 MHz, NE-U17, Omron Healthcare Co., Ltd., Kyoto, Japan) for droplet generation, a tubular furnace, and an electrostatic precipitator, as shown in Figure 1. The tubular furnace consisted of

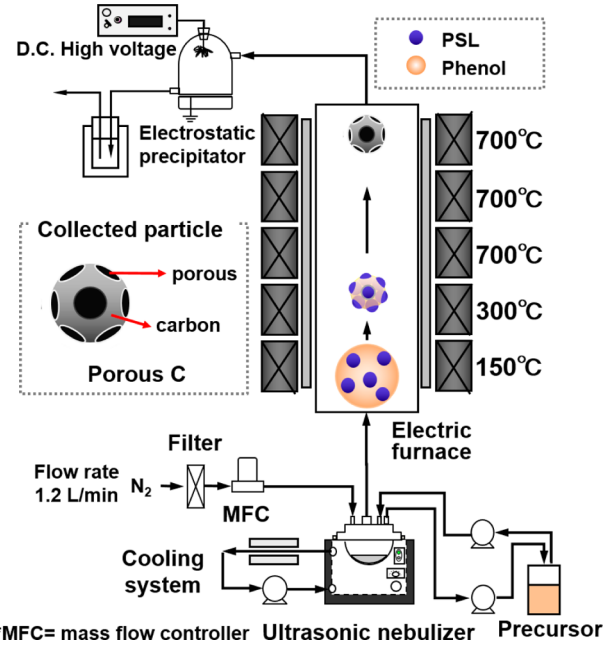

Figure 1. Schematic diagram of the experimental setup.

five stacked temperature zones set at 150, 300, 700, 700, and 700 °C, respectively. The mass ratio of phenolic resin to PSL was 5, 2.5, 1.25, 0.625, and 0.25. The Pt impregnation process has been described in our earlier work.[4] The process was repeated here.

2.2. Characterization. The particle morphology was observed using field-emission scanning electron microscopy (FE-SEM; S-5000, 20 kV, Hitachi High-Tech. Corp., Tokyo, Japan) and transmission electron microscopy (TEM; JEM-2010, 200 kV, JEOL Ltd., Tokyo, Japan). The thermal behaviors of the phenolic resin, the phenol–PSL composite, and PSL were analyzed using thermogravimetric analysis (TGA; TGA-50/51, Shimadzu Corp., Kyoto, Japan). The surface area was determined using Brunauer, Emmet, and Teller (BET) method (BEL Japan, Inc., BELSORP-max, Osaka, Japan). Fourier-transform infrared (FT-IR) spectroscopy was used to investigate the chemical reactions involved in phenol carbonization (Spectrum one, Perkin Elmer Inc., Waltham, MA, USA). The Pt content of the catalyst was measured using inductively coupled plasma mass spectrometry (SPS-3000, Seiko Instrument Inc., Chiba, Japan). The crystal structure was determined using X-ray diffraction (XRD; RINT2000, Rigaku, Tokyo, Japan).

Electrochemical characterization of the prepared catalyst was performed using CV and a rotating disc electrode (RDE; HR-301, Hokuto Denko Corp., Tokyo, Japan). A reversible hydrogen electrode (RHE) was used as the reference electrode for these measurements. Catalyst ink was prepared using a procedure reported elsewhere.[4] The required amount of catalyst ink was transferred to a polished glassy carbon disk (Ø = 5 mm, geometric area = 0.196 cm^2) and dried to form a thin catalyst layer. The measurements were performed at room temperature (~25 °C) using a freshly prepared 0.1 M $HClO_4$ electrolyte solution (Cica-reagent, Kanto Chemical Co., Inc., Japan). A nitrogen gas flow of 100 mL min^{-1} was passed through the electrolyte solution for 30 min before measurements to deoxygenate the environment. CV measurements were obtained by scanning between 0 and 1.2 V vs RHE at a sweep rate of 50 mV s^{-1}. The saturating gas was switched to oxygen for the RDE measurements, and the electrolyte was saturated using the same conditions as those used for the CV measurements. The rotation rates were controlled at 400, 900, 1600, 2500, and 3600 rpm to collect data for Koutecký–Levich plots. Measurements were carried out at sweep rates of 10 mV s^{-1} in a typical polarization program of 0.2 V → 1.2 V. The background current was measured by running the ORR sweep profile without any rotation in nitrogen gas purged 0.1 M $HClO_4$ before the ORR measurements to eliminate any contributions from capacitive current.

3. RESULTS AND DISCUSSION

The thermal behaviors of the phenolic resin, PSL, and phenolic resin–PSL composite were examined at the temperature of 20–800 °C under a nitrogen atmosphere as shown as TGA curves in Figure 2. There were four stages observed in the TGA

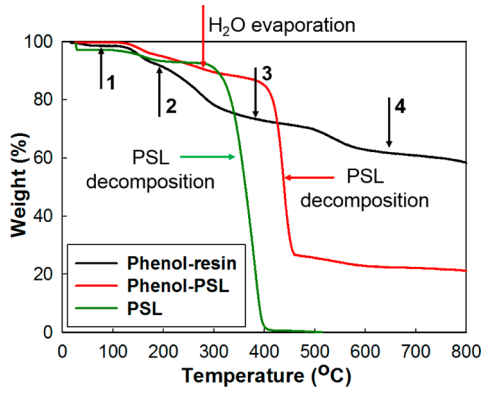

Figure 2. TGA thermograms of the phenolic resin, phenolic resin–PSL composite, and PSL.

curve of the phenolic resin. The first stage was up to 150 °C showed a weight loss of less than ca. 10%. The second and third stages were up to 600 °C indicated two continuous weight decrease and represented the main degradation reaction of ca. 20%. Above 600 °C (the fourth stage) ca. 8% weight loss was observed. The weight loss during this heat treatment is ascribed for the release of various gases (CO, CO_2, CH_4, and H_2) and H_2O evaporation depending on the decomposition state of phenolic resin.[31] The carbonized material was relatively stable in the final step with the lowest weight loss because carbonization had already been achieved. In the case of PSL, the TGA result shows sharp weight degradation at 350 °C and all of the PSL were completely decomposed at 400 °C.

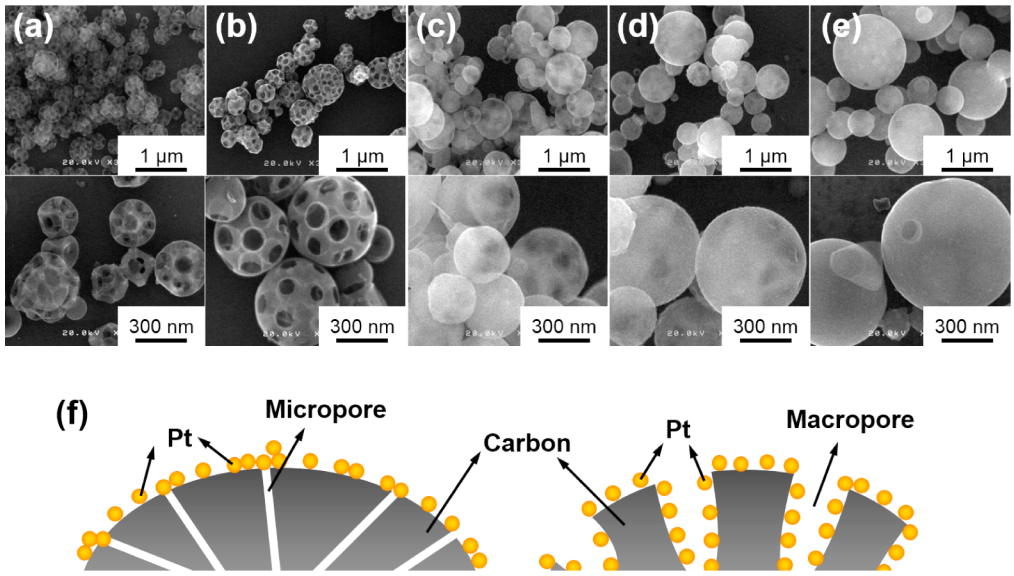

Figure 3. FE-SEM images of porous carbon using 4 wt % P^+ and phenol resin concentrations of (a) 0.1, (b) 0.25, (c) 0.5, (d) 1, and (e) 2 wt %; and (f) schematic diagram of Pt deposition phenomena on the surfaces of microporous and macroporous carbon.

The initial stage of TGA curve of the phenolic resin−PSL composite indicated a similar weight loss as phenolic resin case. However, a sharp weigh loss was observed in the range of 400−450 °C, implying rapid PSL decomposition. A very small decomposition was then presented at 450−600 °C and the weight become stable at the above temperature.

It is to be noted from the TGA results that the large shift of the decomposition temperature of PSL in phenolic resin−PSL composite toward higher temperature ($\Delta T \approx 50$ °C) compared to that of pure PSL particle, indicates the strong interaction formation between phenolic resin and PSL surface. The interaction may be due to the chemical bonding between the OH groups of the phenolic resin and the CN groups on the surface of PSL nanoparticles as described later. Then, the effect of this interaction on the macroporous morphology of carbon particles was examined for several mixing composition by the spray pyrolysis method as follows.

Figure 3 shows the effect of phenolic resin concentration on the carbon particle morphology; the concentration of PSL was fixed at 4 wt % and the amount of phenolic resin was varied, i.e., 0.1, 0.25, 0.5, 1, and 2 wt %. A PSL sol (1 mL) was added per 10 mL of phenolic resin solution. We found that the porosity decreased with increasing amounts of phenolic resin. Similar phenomenon was shown elsewhere.[32] Adjustment of the porous structure of the catalyst support was critical for effective gas/water diffusion and proton/electron transport to and from the catalytic sites without sacrificing the sites for Pt deposition. Figures 3c−e show poorly structured porous morphologies, which tend to be dense when the amount of phenolic resin is high. This provides many sites for Pt deposition on the outer surfaces of the carbon particles, but not on the inner surfaces because the pore sizes of the carbon particles are unsuitable and inhibit Pt ion penetration. Low phenolic resin concentrations gave good catalyst support as a result of the presence of pore channels, as shown in images a and b in Figure 3. The highest porosity of the carbon particles was obtained at a phenolic resin concentration of 0.1 wt %, as shown in Figure 3a. This enables the best fluid transport through the catalytic sites. However, since most of the carbon surface was occupied by macropores, there were only a small number of sites that could be used for Pt deposition. Furthermore, the Pt nanoparticles potentially agglomerate during the deposition process. The optimum porous morphology was obtained at a phenolic resin concentration of 0.25 wt %, as shown in Figure 3b. This porous morphology provided a good combination of fluid transport and Pt deposition sites. Fluid transport occurs effectively and Pt can be deposited both on the outer and inner surfaces of the carbon, which means that a higher number of active catalytic sites can be achieved. The specific surface area (S_{BET}) of this porous carbon was 107 m^2 g^{-1}. Figure 3f shows the probable phenomena that occur during Pt deposition on the surface of microporous and macroporous carbon.

The beautiful formation of self-organized macroporous carbon obtained at a phenolic resin concentration of 0.25 wt %, as shown in Figure 3b may be due to the chemical interaction between phenolic resin and PSL. Therefore, the chemical structure of porous-carbonized sample and the PSL were further investigated. FT-IR spectra were obtained and are shown in Figure 4. In the FT-IR spectrum of PSL, alkyl (C_nH_{2n+1}) groups were found in the range of 600−1000 and 1400−1700 cm^{-1}. Sharp peak at 3033 cm^{-1} and double peaks at 2921 and 2848 cm^{-1} correspond to the C−H stretching

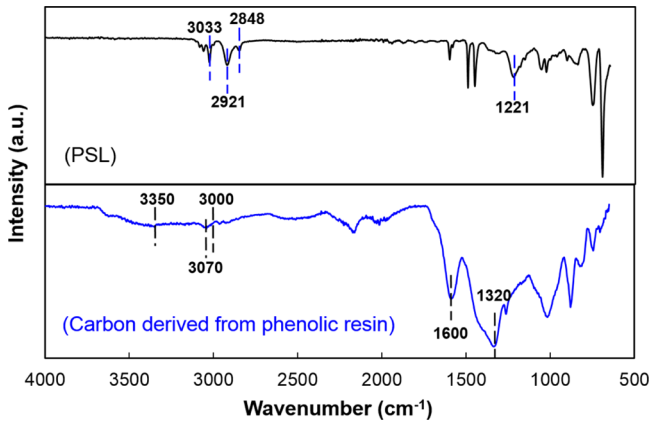

Figure 4. FT-IR spectra of the PSL and phenolic resin derived carbon.

mode. Polar group of C−N stretch was indicated by peak at 1221 cm^{-1}. In the case of porous-carbonized sample, a weak broad peak was observed at 3350 cm^{-1}, indicating the presence of OH···OH, OH···O (ether oxygen), or OH···O═C hydrogen bonds. An aromatic bond from benzene was indicated by a weak peak at 3070 cm^{-1}. The weak peak at 3000 cm^{-1} indicated the presence of −OH bonds. An aromatic ring C−C bond was also present as indicated by the strong peak at 1600 cm^{-1}. A strong peak at 1320 cm^{-1} that corresponds to a C−O stretching vibration was found for the carbonized sample.[31,33,34] This peak is not present in Vulcan XC-72 carbon, as reported by Li et al.[35] This peak shows that a large amount of unsaturated carbon atoms are present and these are highly active toward reaction with oxygen and form oxygen-containing group that may enhance the ORR activity.[35] These results indicated that the interaction between PSL and phenolic resin is due to the hydrogen bonding and electrostatic bonding among polar groups such as C−N, −OH, and C═O groups.

Functionalization of porous carbon as a catalyst support was performed by Pt impregnation (~20 wt %) to the porous carbon surface, and was mediated by PVA. Images a and b in Figure 5 show FE-SEM images of the porous Pt/C particles. These images confirm the presence of Pt nanoparticles on the porous carbon surfaces and show that the carbon particles have strong structures and their morphology is maintained as spherical porous particles after Pt deposition. The carbon particles have well-structured pores with specific angles and, interestingly, agglomeration-free Pt nanoparticles deposited on the inner surfaces of the carbon particles and in the cavities, as shown clearly by the TEM images in Figure 5(c) and (d). Figure 5(e) confirms that the deposited Pt is well-dispersed. The surfaces of the deposited Pt nanoparticles are clean and the nanoparticles form a crystal structure, as shown by the clear lattice spacing. The mean diameters of the Pt nanoparticles were calculated using 280 Pt nanoparticles and found to be 3.91 nm with a standard deviation of about 0.67 nm, as shown by the histogram in Figure 5(f). The amount of Pt nanoparticles in the porous carbon was confirmed by ICP measurements and found to be 18.9 wt %, which is slightly different to that in the prepared precursor. Small amounts of Pt were lost during Pt deposition and washing.

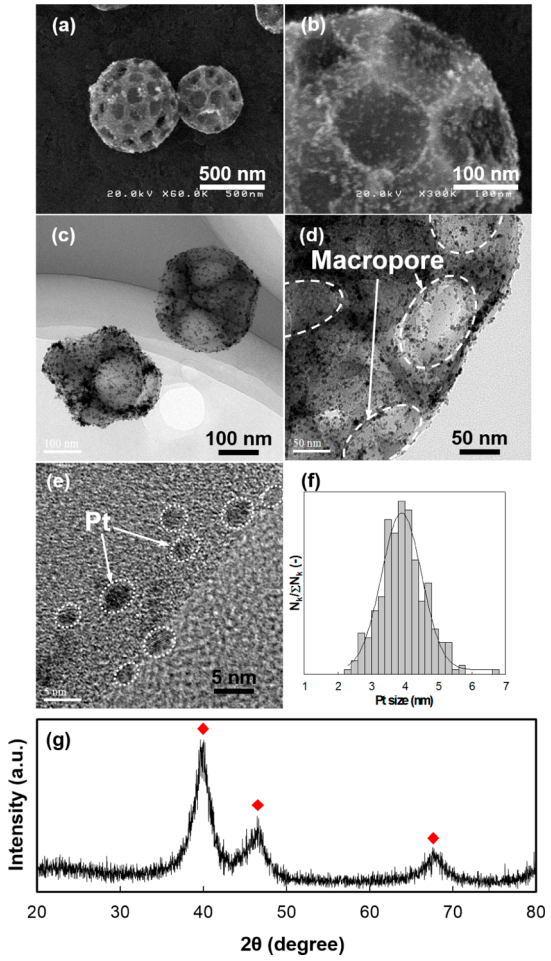

Figure 5. (a, b) FE-SEM images of the porous Pt/C catalyst, (c, d) TEM images of the porous Pt/C catalyst, (e) HR-TEM image of the distribution of 20 wt % Pt on the carbon surface, (f) histogram of Pt nanoparticle distribution, and (g) XRD pattern of the porous Pt/C catalyst after reheating at 120 °C for 120 min under vacuum.

Figure 5(g) shows the XRD pattern of the porous Pt/C catalyst. The XRD pattern has broad peaks at 25° (2θ) corresponding to the diffraction of amorphous carbon. The diffraction peaks of Pt are present at 39°, 46°, and 68° (2θ), which corresponds to the (111), (200), and (220) crystalline planes, respectively (JCPDS Card No. 4-0802), with a face-centered cubic crystal structure. The crystallite size of the Pt nanoparticles was calculated using the Scherrer equation and found to be 4.21 nm. The Pt crystallite size was almost equal to the Pt nanoparticle diameter; this was calculated using the TEM images. The Pt diffraction peaks proved that the reduction of chloroplatinic acid by sodium borohydride had been achieved.

To discover the effect of catalyst support pore size to the Pt deposition, we also deposited Pt nanoparticles on the microporous carbon. The obtained deposition phenomena was totally different from that of on the macroporous carbon, as shown from the FE-SEM images of Figure 6. Pt nanoparticles were growth locally and highly agglomerated. Even though microporous Pt/C catalysts were prepared using exactly the same method as macroporous Pt/C, and the amount of Pt loading was also the same ~20 wt %. This phenomenon agreed the previous prediction on the effect of catalyst support pores to the Pt nanoparticles deposition that was presented in Figure 3f.

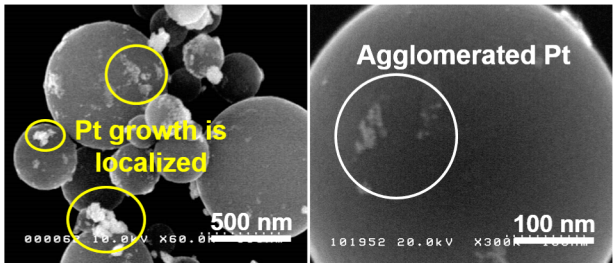

Figure 6. FE-SEM images of microporous Pt/C catalyst.

Electron tomography (ET) images of the porous Pt/C catalyst are shown in Figure 7. The red, green, and blue axes represent the *x*-, *y*-, and *z*-axes, respectively. The presence of C and Pt atoms in the observed particles are shown in blue and red, respectively, whereas green shows the transition from each Pt area to C area. Figure 7a shows that the catalyst is highly porous and the pores have an interconnected system.

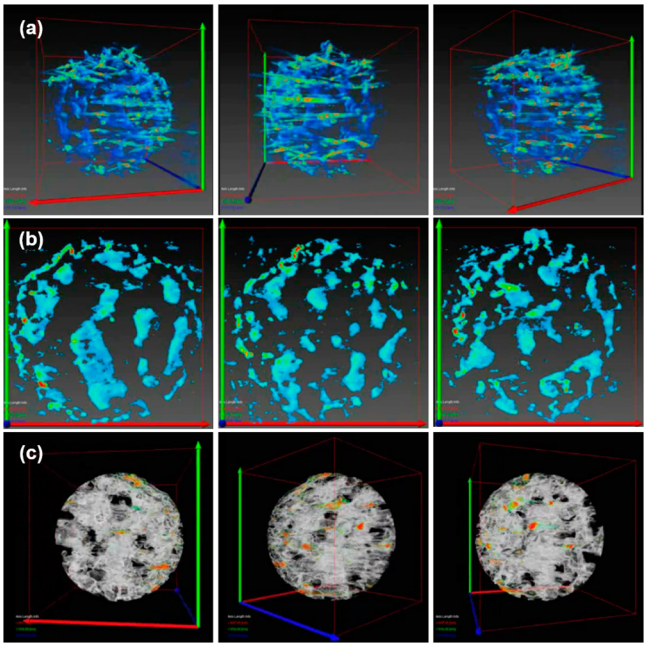

Figure 7. Electron tomography (ET) images of the porous Pt/C catalyst: (a) in the *x*, *y*, and *z* directions, (b) in the *x* and *y* directions, and (c) after the reconstruction process.

Furthermore, Pt nanoparticles were well-dispersed over the entire carbon surface including the inside of the pores. A slice of the ET image taken at $z = r$ (r is the radius of the observed sample) is shown in Figure 7b. It is clear that pore space is present inside the catalyst. This observation confirms that the prepared porous catalyst offers effective fluid transport and it may also have an enhanced Pt nanoparticles active surface. Figure 7c shows reconstructed 3D-TEM images of the synthesized porous Pt/C catalyst. This image shows that the catalyst particle contained macropores in addition to many small pores that clog each other and form a layer with "crumpled graphene-like" morphology. This is advantageous from an active surface area point of view and another reason why Pt nanoparticles are well-dispersed in this catalyst support.

The electrochemical properties of the prepared porous Pt/C catalyst were determined using CV and ORR polarization curves. In addition, the electrochemical properties of a commercial Pt/C catalyst (46.1 wt %, purchased from Tanaka Kikinzoku Kogyo Co., Ltd., Tokyo, Japan) were also evaluated to determine the figure of merit of the prepared catalyst. Figure 8a shows the typical hydrogen adsorption/desorption characteristics of both porous Pt/C and commercial Pt/C at the 10th measurement cycle. The electrochemically active surface areas (ECSAs) of Pt in the working electrode were found to be 81.78 and 80.47 $m^2\ g^{-1}$-Pt for the prepared and the commercial catalyst, respectively. The ECSAs were calculated using the hydrogen adsorption charge ($Q_{H\text{-adsorption}}$) area limited by the minimum potential, which was just above the potential of H_2 generation onset (between 0.07 to 0.4 V vs RHE). The prepared catalyst had a comparable ECSA even though the Pt loading was much less than that of the commercial catalyst. In addition, the Pt size of the prepared catalyst (~3.9 nm) was twice that of the commercial catalyst (~2 nm).

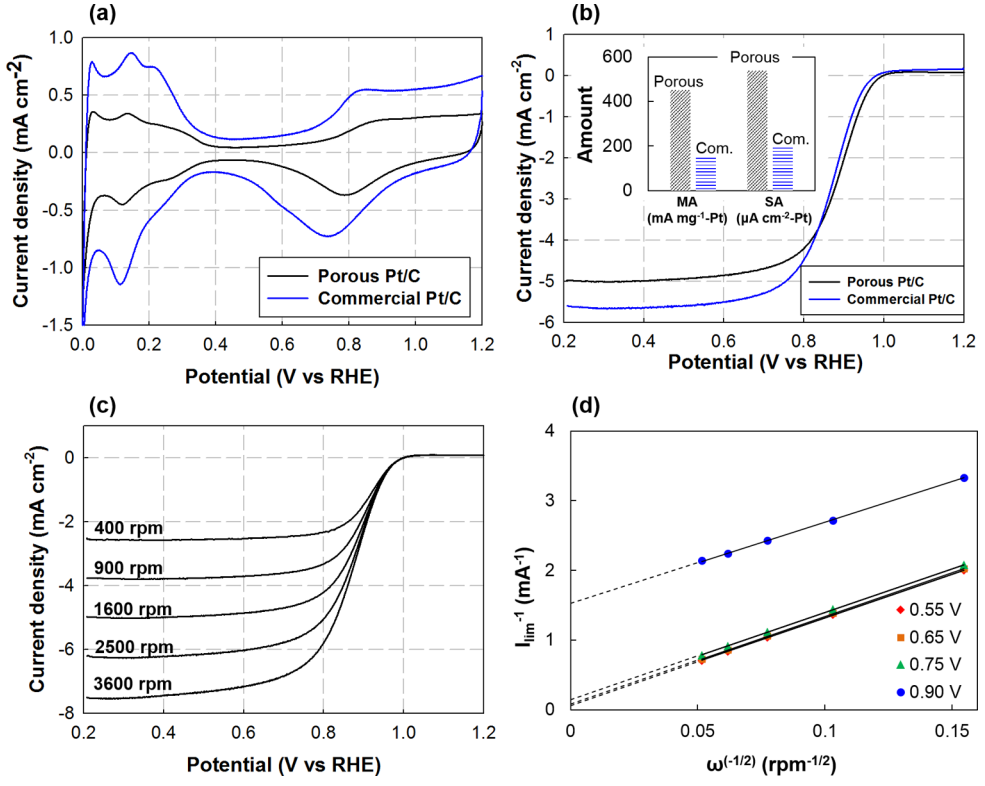

Figure 8. (a) CVs of the porous Pt/C catalyst and the commercial Pt/C catalyst over 10 cycles in oxygen-free 0.1 M $HClO_4$ (cycling between 0 and 1.2 V at 50 mV s^{-1} sweep rate), (b) comparison of the ORR polarization curves of the porous Pt/C catalyst and the commercial Pt/C catalyst at a rotation rate of 1600 rpm, (c) ORR polarization curves at different rotation rates for the porous Pt/C catalyst after 10 cycles in oxygen-saturated 0.1 M $HClO_4$ at a sweep rate of 10 mV s^{-1}, and (d) Koutecký-Levich plots of the porous Pt/C catalyst at different rotation rates and potentials.

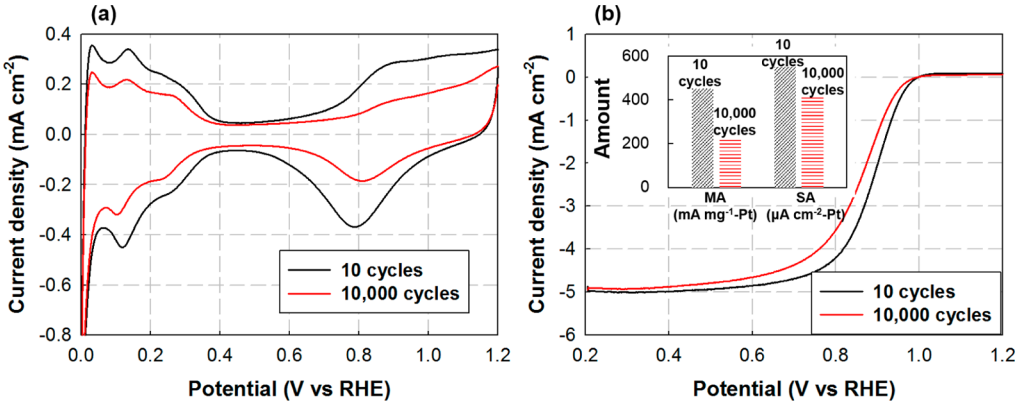

Figure 9. (a) CVs of the porous Pt/C catalyst over 10 and 10 000 cycles in oxygen-free 0.1 M $HClO_4$ (cycling between 0 and 1.2 V at 50 mV s^{-1} sweep rate), (b) ORR polarization curves of the porous Pt/C catalyst over 10 and 10 000 cycles at a rotation rate of 1600 rpm.

Typical ORR curves of the prepared and commercial Pt/C catalyst, measured after the 10th CV cycle are shown in Figure 8b. The ORR curves for the porous Pt/C recorded at different rotation speeds are shown in Figure 8c. These measurements were performed to obtain Koutecký–Levich plots (Figure 8d) to calculate the number of electrons transferred during O_2 reduction and to evaluate the mass and specific activities using the limiting current method. The target potential for the calculation of the mass activity and the specific activity was quantified at E = 0.9 V. The number of electrons involved in the ORR was calculated using the Koutecký–Levich equation and 4 electrons were involved for both the prepared porous Pt/C and the commercial Pt/C catalyst. Pt mass activity values were calculated by normalizing the Pt loading on the disk electrode and the specific activity values were estimated by calculating the mass–specific activities and normalizing them to the Pt ECSA. The high-quality of the catalyst is shown by its high electrocatalytic activity. The mass activity value under the initial condition (10 cycles) was 450.81 mA mg^{-1}-Pt, whereas the specific activity value was 551.24 μA cm^{-2}-Pt. These values were twice those of the commercial Pt/C catalyst, which was about 155.00 mA mg^{-1}-Pt and 192.61 μA cm^{-2}-Pt for the mass activity and the specific activity, respectively. The values for the mass activities and the specific activities of the prepared sample and the commercial Pt/C are summarized in the inset of Figure 8b.

Electrocatalytic activity measurements for both catalysts were conducted over 10,000 cycles to determine their durability. Over the first 1000 cycles the porous Pt/C had a relatively more stable ECSA than the commercial catalyst with total degradations of 23.45 and 29.51% for porous Pt/C and commercial Pt/C, respectively. Because the performance of the commercial Pt/C was already low in this step, only the porous Pt/C catalyst was used for further durability testing. Typical CV polarization curves of the prepared catalyst at the 10th and 10 000th cycles are shown in Figure 9. The CV curve at the 10 000th cycle was smaller than that measured at the 10th cycle. However, there was no change in the shape of the polarization curve showing that hydrogen adsorption/desorption still took place even at the 10 000th cycle. This means that there are no significant carbon particle breakages during the durability measurements even though some Pt agglomeration occurred. After 10 000 cycles, the ECSA only decreased by 35.17% and its value was 53.11 m^2 g^{-1}-Pt. The mass activity and specific activity were 219.43 mA mg^{-1}-Pt and 413.20 μA cm^{-2}-Pt, respectively. Although a fairly high level of degradation was evident the electrocatalytic activity values were still higher than those of the commercial catalyst. This phenomenon proves that phenolic resin-derived carbon has good durability under acidic conditions. Phenolic resin- derived carbon may have strong corrosion resistance that maintains the active catalyst.

The 3.91 nm particle size observed on the as-prepared porous carbon supports is large compared with those typically observed on commercial carbon (~2 nm). This finding suggests that Pt size is not the only important requirement to obtain high electrocatalytic activity. Carbon as a catalyst support also plays a role and is as important as the Pt catalyst. Carbon derived from phenolic resin, which contains various aromatic structures exhibits good electronic conductivity.[28] The obtained carbon morphology also consists of several layers, which increases the active surface area. A combination of the above two factors and the control of morphology to give macroporous–nanosphere particles increases the electrical conductivity of the prepared catalyst, and the above findings are first discussed in this work.

4. CONCLUSION

This study demonstrated a facile strategy for the production of a novel electrocatalyst support material, i.e., porous carbon derived from phenolic resin using spray pyrolysis. The morphology of the phenolic resin derived carbon was controlled simply by the addition of appropriate amount of PSL template particles to the precursor. Pt deposition on the phenolic resin derived carbon was achieved using a standard industrial impregnation method. Agglomeration-free and well-dispersed Pt nanoparticles of average size 3.91 nm were observed on the surfaces of the porous carbon particles. The high performance of the porous Pt/C electrocatalyst was proven by its high mass activity and electrochemically active surface area, which were 450.81 mA mg^{-1}-Pt and 81.78 m^2 g^{-1}-Pt, respectively. The porous Pt/C mass activity value is twice those of the available commercial Pt/C catalyst.

AUTHOR INFORMATION

Corresponding Author

*E-mail: ogit@hiroshima-u.ac.jp. Phone: +81-82-424-7850. Fax: +81-82-424-7850.

Notes

The authors declare no competing financial interest.

■ ACKNOWLEDGMENTS

This research was supported by a Grant-in-Aid for Young Scientists (B) (No. 23760729) and a Grant-in-Aid for Scientific Research (A) (22246099), sponsored by the Ministry of Education, Culture, Sports, Science and Technology of Japan. The Japan Society for the Promotion of Science (JSPS) is gratefully acknowledged for providing a fellowship for R.B. The authors thank Dr. Eishi Tanabe from the Hiroshima Prefectural Institute of Industrial Science and Technology for helping with the TEM analysis and the Sumitomo Bakelite Co., Ltd., for supplying the phenolic resin.

■ REFERENCES

(1) Chang, H.; Joo, S. H.; Pak, C. *J. Mater. Chem.* **2007**, *17*, 3078−3088.
(2) Zhang, S.; Shao, Y.; Yina, G.; Lin, Y. *J. Mater. Chem. A* **2013**, *1*, 4631−4641.
(3) Antolini, E. *Appl. Catal., B* **2009**, *88*, 1−24.
(4) Balgis, R. B.; Anilkumar, G. M.; Sago, S.; Ogi, T.; Okuyama, K. *J. Power Sources* **2012**, *203*, 26−33.
(5) Balgis, R. B.; Anilkumar, G. M.; Sago, S.; Ogi, T.; Okuyama, K. *Fuel Cells* **2012**, *12*, 665−669.
(6) Balgis, R. B.; Anilkumar, G. M.; Sago, S.; Ogi, T.; Okuyama, K. *J. Power Sources* **2013**, *229*, 58−64.
(7) Joo, S. H.; Choi, S. J.; Oh, I.; Kwak, J.; Liu, Z.; Terasaki, O.; Ryoo, R. *Nature* **2001**, *412*, 169−172.
(8) Kou, R.; Shao, Y.; Mei, D.; Nie, Z.; Wang, D.; Wang, C.; Viswanathan, V. V.; Park, S.; Aksay, I. A.; Lin, Y.; Wang, Y.; Liu, J. *J. Am. Chem. Soc.* **2011**, *133*, 2541−2547.
(9) Zheng, Y.; Jiao, Y.; Chen, J.; Liu, J.; Du, A.; Zhang, W.; Zhu, Z.; Smith, S. C.; Jaroniec, M.; Lu, G. Q.; Qiao, S. Z. *J. Am. Chem. Soc.* **2011**, *133*, 20116−20119.
(10) Suryamas, A. B.; Anilkumar, G. M.; Sago, S.; Ogi, T.; Okuyama, K. *Catal. Commun.* **2013**, *33*, 11−14.
(11) Kakinuma, K.; Wakasugi, Y.; Uchida, M.; Kamino, T.; Uchida, H.; Deki, S.; Watanabe, M. *Electrochim. Acta* **2012**, *77*, 279−284.
(12) Ogi, T.; Balgis, R.; Okuyama, K.; Tajima, N.; Setyawan, H. *AIChE J.* **2013**, *59*, 2753−2760.
(13) Avasarala, B.; Murray, T.; Li, W.; Haldar, P. *J. Mater. Chem.* **2009**, *19*, 1803−1805.
(14) Chang, H.; Joo, S. H.; Pak, C. *J. Mater. Chem.* **2007**, *17*, 3078−3088.
(15) Xu, S.; Qiao, G.; Wang, H.; Li, D.; Lu, T. *Mater. Lett.* **2008**, *62*, 3716−3718.
(16) Fang, B.; Chaudhari, N. K.; Kim, M.-S.; Kim, J. H.; Yu, J.-S. *J. Am. Chem. Soc.* **2009**, *131*, 15330−15338.
(17) Garsany, Y.; Epshteyn, A.; Purdy, A. P.; More, K. L.; Swider-Lyons, K. E. *J. Phys. Chem. Lett.* **2010**, *1*, 1977−1981.
(18) Koenigsmann, C.; Santulli, A. C.; Gong, K.; Vukmirovic, M. B.; Zhou, W.-P.; Sutter, E.; Wong, S. S; Adzic, R. R. *J. Am. Chem. Soc.* **2011**, *133*, 9783−9795.
(19) Rolison, D. R. *Science* **2003**, *299*, 1698−1701.
(20) Güvenatama, B.; Fıçıcılar, B.; Bayrakçekenb, A.; Eroğlu, I. *Int. J. Hydrogen Energy* **2012**, *37*, 1865−1874.
(21) Liang, C.; Li, Z.; Dai, S. *Angew. Chem., Int. Ed.* **2008**, *47*, 3696−3717.
(22) Wang, Z.; Li, F.; Ergang, N. S.; Stein, A. *Chem. Mater.* **2006**, *18*, 5543−5553.
(23) Yoo, H.; Moon, J. H. *RSC Adv.* **2012**, *2*, 8934−8936.
(24) Hu, B.; Wang, K.; Wu, L.; Yu, S.-H.; Antonietti, M.; Titirici, M. M. *Adv. Mater.* **2010**, *22*, 813−828.
(25) Inagaki, M.; Orikasab, H.; Morishita, T. *RSC Adv.* **2011**, *1*, 1620−1640.
(26) Liang, C.; Dai, S. *J. Am. Chem. Soc.* **2006**, *128*, 5316−5317.
(27) Ryu, J.; Suh, Y.-W.; Suh, D. J.; Ahn, D. J. *Carbon* **2010**, *48*, 1990−1998.
(28) Guan, G.; Kusakabe, K.; Ozono, H.; Taneda, M.; Uehara, M.; Maeda, H. *J. Mater. Sci.* **2007**, *42*, 10196−10202.
(29) Xue, X.; Lu, T.; Liu, C.; Xing, W. *Chem. Commun.* **2005**, 1601−1603.
(30) Yu, X.; Ding, S.; Meng, Z.; Liu, J.; Qu, X.; Lu, Y.; Yang, Z. *Colloid Polym. Sci.* **2008**, *286*, 1361−1368.
(31) Kim, Y. J.; Kim, M. I.; Yun, C. H.; Chang, J. Y.; Park, C. R.; Inagaki, M. *J. Colloid Interface Sci.* **2004**, *274*, 555−562.
(32) Nandiyanto, A. B. D.; Arutanti, O.; Ogi, T.; Iskandar, F.; Kim, T. O.; Okuyama, K. *Chem. Eng. Sci.* **2013**, *101*, 523−532.
(33) Li, J.-G.; Chung, C,-Y.; Kuo, S.-W. *J. Mater. Chem.* **2012**, *22*, 18583−18595.
(34) Wu, Z.; Meng, Y.; Zhao, D. *Microporous Mesoporous Mater* **2010**, *128*, 165−179.
(35) Li, Y.; Wang, J.; Geng, D.; Li, R.; Sun, X. *Chem. Commun.* **2011**, *47*, 9438−9440.